

# Thermodynamic properties on the homologous temperature scale from direct upsampling: Understanding electron-vibration coupling and thermal vacancies in bcc refractory metals

Axel Forslund <sup>\*</sup>, Jong Hyun Jung , Prashanth Srinivasan , and Blazej Grabowski 

*Institute for Materials Science, University of Stuttgart, Pfaffenwaldring 55, 70569 Stuttgart, Germany*



(Received 3 February 2023; accepted 4 May 2023; published 22 May 2023)

We have calculated thermodynamic properties of four bcc refractory elements—V, Ta, Mo, and W—up to the melting point with full density-functional-theory accuracy, using the recently developed direct-upsampling method [J. H. Jung *et al.*, *npj Comput. Mater.* **9**, 3 (2023)]. The direct-upsampling methodology takes full account of explicit anharmonic vibrations and electron-vibration coupling very efficiently using machine-learning potentials. We have thus been able to compute highly converged free-energy surfaces for the PBE exchange-correlation functional, from which accurate temperature dependencies of various thermodynamic properties such as the heat capacity, thermal expansion coefficient, and bulk modulus are accessible. For all four elements, the electronic contribution is large, including a strong coupling with the thermal vibrations. The atomic forces in W are even affected by the temperature-consistent Fermi broadening, which alters the free energy by around 3 meV/atom at the melting point. Trends within group V and group VI refractory elements are observed and explained by qualitative differences in the electronic density of states. We also provide an estimate of the Gibbs energies of vacancy formation and the vacancy contribution to the thermodynamics. Lastly and most importantly, our results are analyzed in terms of the homologous temperature scale relative to theoretically predicted melting points (for the PBE functional). The homologous temperature dependencies show a remarkable agreement with experiments and reveal the predictive power of self-consistently determined *ab initio* thermodynamic properties.

DOI: [10.1103/PhysRevB.107.174309](https://doi.org/10.1103/PhysRevB.107.174309)

## I. INTRODUCTION

The bcc refractory elements are characterized by very high melting points, generally above 2000 °C (2273 K), high densities, and hardness, making them appropriate for a wide range of applications [1–5]. Their high radiation resistance renders them potential candidates for nuclear reactor design [6]. In addition to the unary elements, refractory alloys such as NbMoTaVW and TaVCrW are also used in similar applications. A crucial requisite for materials design for such applications is accurate high-temperature thermodynamic data of the unary systems. With precise knowledge of the end members, one can also design phase diagrams of refractory high-entropy alloys [7].

Despite the importance of the refractory metals, and the experimental difficulties in measuring high-temperature properties, there have been relatively few attempts to computationally model their unaries from first principles. A compilation of the available studies that include temperature-dependent thermodynamic properties is presented in Table I. Most of the previous studies focused on W and Ta, reporting results within the quasiharmonic (QH) approximation. While the QH approximation is computationally inexpensive for simple unary systems, it neglects anharmonic vibrational effects [8], particularly important for bcc systems [9]. An advancement over the standard 0 K QH approximation is to consider effective harmonic Hamiltonians [10] or

renormalized phonon dispersions [11,12] fitted to molecular dynamics at higher temperature. However, for bcc refractory systems, even the use of such effective approaches cannot fully account for the strong anharmonic effects [9,13].

Over the last decade, thermodynamic integration (TI)-based techniques have been developed to accurately predict properties up to high temperatures to density-functional-theory (DFT) accuracy [8,27–29], including anharmonic, electronic, and coupling effects. The emergence of machine-learning interatomic potentials further reduced computational costs [13,30,31] and allowed for accurate calculations even for complex structures [26]. Most recently, as a culmination of the prior TI techniques, a streamlined procedure—the *direct-upsampling* approach—was suggested [32], providing an efficient and relatively straightforward way of computing thermodynamic properties up to the melting point.

The direct-upsampling method combines machine-learning moment tensor potentials (MTPs) [33] with TI and free-energy perturbation (FEP) theory [34]. Out of the four unary systems whose thermodynamic properties were calculated with direct upsampling previously [32], niobium (Nb) was the most challenging, with its high electronic contribution, electron-vibration coupling, and high melting temperature. The resulting thermodynamic properties were in good agreement with experimental results. Nonetheless, the electron-vibration coupling was not investigated explicitly, the contribution of vacancies (potentially noticeable at high temperatures) was not considered, and the inherent error due to the exchange-correlation (XC) functional lead to some deviation from experiments.

<sup>\*</sup>axel.forslund@imw.uni-stuttgart.de

TABLE I. *Ab initio* studies of the isobaric heat capacity ( $C_p$ ), the thermal expansion coefficient ( $\alpha$ ) and the bulk modulus ( $B$ ) for bcc V, Ta, Mo, and W. The corresponding XC functionals and the potentials representing the core electrons are listed. The columns under “Contributions to  $F$ ” indicate which terms (0 K static energy “ $E_{0K}$ ”, electronic “el”, quasiharmonic “qh”, and anharmonic “ah”) were included to the total free energy. For works that included an anharmonic contribution, the number of volume  $V$  and temperature  $T$  data points is mentioned. Studies including the explicit anharmonic contribution up to all orders and to the accuracy of DFT are printed in boldface. The last three columns indicate whether a heat capacity, expansion coefficient, or bulk modulus was presented including anharmonic contributions. All of the used abbreviations are expanded in the Supplemental Material [14].

Year	Ref.	Elements	DFT methodology		Contributions to $F$								
			XC	Potential	$E_{0K}$	el	qh	ah	Grid for ah	$C_p^{\text{ah}}$	$\alpha^{\text{ah}}$	$B^{\text{ah}}$	
2001	[15]	bcc W	LDA	NC	x		x						
2006	[16]	bcc Ta	PBE	FP-LMTO	x	x	x						
2006	[17]	bcc Ta	LDA	PAW	x		x	SMM					
2006	[18]	bcc V	PBE	LMTO	x	x	x						
2008	[19]	bcc Mo	LDA/PBE	FP-LMTO	x	x	x						
2009	[20]	bcc Ta	PBE	US	x	x	x						
2009	[21]	bcc Ta	PBE	PAW				thermal pressure	$14V \times 7T$		x		
2010	[22]	bcc Mo	PW91	US	x	x	x						
2016	[23]	bcc W	PBE	US	x	x	x						
2017	[24]	bcc W	PBEsol	PAW	x	x	x						
2021	[25]	bcc W	PBE	PAW	x		x						
2022	[26]	bcc W	PBEsol	PAW	x	x	x	<b>TU-TILD+MTP</b>	$5V \times 13T$	x			x
2023	this paper	bcc V, Ta, Mo, W	PBE	PAW	x	x	x	<b>direct upsampling</b>	$\geq 10V \times 11T$	x	x		x

In the present paper, we address all of the above challenges, thereby further evolving the direct-upsampling methodology and the knowledge on high-temperature thermodynamic properties. We do so by considering four other refractory elements vanadium (V), tantalum (Ta), molybdenum (Mo), and tungsten (W), which are expected to pose similar challenges as Nb. We perform free-energy calculations on very dense volume-temperature grids—a necessity for highly converged thermodynamic properties up to the melting point—within the PerdewBurke-Ernzerhof (PBE) [35] XC functional. We analyze in detail the effect of the electronic temperature on the molecular dynamics (MD) forces. We break down both the temperature-dependent vibrational and electronic free energies into a “pure” and a “coupling” part and study the separate impact of the vibrations and thermal electronic excitations on the free energies as well as their mutual interaction. We attempt to compensate for the inherent error in the XC functional by using a homologous temperature scale relative to the PBE-predicted melting temperature. Additionally, we estimate temperature-dependent vacancy formation Gibbs energies, and evaluate their contribution to the thermodynamic properties. Finally, we investigate the robustness of the TI, in terms of stability maps showing the probability to encounter vacancy diffusion and Frenkel defect formation.

## II. METHODS

In order to numerically derive thermodynamic properties, we calculate the total free-energy surface for the four bcc refractory elements (V, Ta, Mo, and W). The free energies are obtained using the recently developed direct-upsampling methodology on a highly dense volume-temperature ( $V, T$ ) grid. An analysis of the direct-upsampling methodology can be found in Ref. [32], with a detailed description of the procedure provided in the Supplementary Information to Ref. [32].

The free energy is adiabatically decomposed as [36]

$$F(V, T) = E_{0K}(V) + F^{\text{el}}(V, T) + F^{\text{qh}}(V, T) + F^{\text{ah}}(V, T). \quad (1)$$

Here,  $E_{0K}(V)$  represents the energy-volume ( $E - V$ ) curve at 0 K,  $F^{\text{el}}(V, T)$  the electronic free energy,  $F^{\text{qh}}(V, T)$  an effective QH free energy, and  $F^{\text{ah}}(V, T)$  the (remaining) anharmonic contribution. The last two terms constitute the vibrational free energy of the ions,  $F^{\text{vib}}(V, T) = F^{\text{qh}}(V, T) + F^{\text{ah}}(V, T)$ . Once computed via direct upsampling, the free-energy surface is Legendre transformed to obtain the Gibbs energy  $G(p, T)$  at a pressure  $p$  as

$$G(p, T) = F(V, T) + pV, \quad (2)$$

from which all thermodynamic properties can be obtained using well-known thermodynamic relations [32].

The electronic free energy can be considerably affected by thermal vibrations [37]. Likewise, the thermal ionic vibrations can experience a change by the thermal electronic excitations, although the effect is expected to be marginal. One aim of the present study is to evaluate, in particular, the latter coupling effect. The direct-upsampling methodology as described in Ref. [32] is well suited for that purpose as it accounts for all relevant terms: the full vibrational free energy including explicit anharmonic contributions, the electronic free-energy contribution through finite-temperature DFT [38], and the respective coupling contributions between ions and electrons. The details of the exact relations are given in Sec. II A.

Another aim of our paper is to evaluate the impact of thermal, noninteracting vacancies on the bulk thermodynamics. The direct-upsampling methodology is well suited for that purpose as well. Specifically, in addition to the perfect bulk, the Gibbs energy of a vacancy-containing supercell needs to be computed including the free energy terms as given

in Eq. (1). From the difference of the Gibbs energies of the vacancy-containing supercell and the perfect bulk (with proper normalization factors), the Gibbs energy of vacancy formation  $G_{\text{vac}}^f$  can be obtained. The contribution to the bulk thermodynamics is then given by

$$G(p, T) = G_{\text{perf}}(p, T) - k_B T \exp \left[ -\frac{G_{\text{vac}}^f(p, T)}{k_B T} \right], \quad (3)$$

where  $G_{\text{perf}}(p, T)$  is the Gibbs energy of the ideal perfect bulk without vacancies. The details of how we proceed in this respect are given in Sec. II B.

### A. Electron-vibration coupling terms

For the analysis and the discussion of the coupling terms, it is useful to have specific expressions available. To derive those, we write the free-energy difference  $\Delta F$  between the QH reference (without thermal electronic excitations) and the fully anharmonic DFT system as

$$\Delta F(T) = \int d\mathcal{R} d\lambda \rho(\mathcal{R}; \lambda, T) \Delta E(\mathcal{R}; T), \quad (4)$$

where  $\mathcal{R} = \{\mathbf{R}_I\}$  denotes the set of atomic coordinates  $\mathbf{R}_I$ ,  $\lambda$  the coupling parameter between the QH and anharmonic system,  $\rho(\mathcal{R}; \lambda, T)$  the probability distribution in configuration space, and  $\Delta E(\mathcal{R}; T)$  the energy difference between the QH and anharmonic system for a particular ionic configuration. The integral in Eq. (4) is multidimensional and includes an integral over  $\lambda$  (from zero to one) and an integral over the configuration space for each  $\lambda$ .

As defined,  $\Delta F$  in Eq. (4) takes all thermodynamic effects related to anharmonic vibrations and electronic excitations into account and equals the sum of  $F^{\text{el}} + F^{\text{ah}}$  in Eq. (1). However, the formulation in Eq. (4) is better suited to derive explicit expressions for the coupling terms. To this end, we introduce two temperatures,  $T_{\text{ion}}$  and  $T_{\text{el}}$ , where  $T_{\text{ion}}$  corresponds to the thermal vibrations of the ions and  $T_{\text{el}}$  to the broadening of the Fermi-Dirac distribution of the electrons. With these, we rewrite Eq. (4) as

$$\Delta F(T_{\text{ion}}, T_{\text{el}}) = \int d\mathcal{R} d\lambda \rho(\mathcal{R}; \lambda, T_{\text{ion}}, T_{\text{el}}) \Delta E(\mathcal{R}; T_{\text{el}}). \quad (5)$$

Note that the probability density  $\rho$  depends on both  $T_{\text{ion}}$  and  $T_{\text{el}}$ . In the actual calculations,  $\rho$  is determined via MD and thus via the forces acting on the atoms. The forces are controlled by the thermostat with which we associate the temperature  $T_{\text{ion}}$  and they can additionally be affected by the electron excitations, i.e., by  $T_{\text{el}}$ . In contrast to  $\rho$ , the energy difference  $\Delta E$  depends only on the Fermi broadening.

Next, we decompose  $\Delta F$  into “pure” and “coupling” contributions as follows. For the pure contributions we write

$${}^{\circ}F^{\text{ah}}(T_{\text{ion}}) = \int d\mathcal{R} d\lambda \rho(\mathcal{R}; \lambda, T_{\text{ion}}, T_{\text{el}} = 0) \Delta E(\mathcal{R}; T_{\text{el}} = 0), \quad (6)$$

and

$${}^{\circ}F^{\text{el}}(T_{\text{el}}) = \int d\mathcal{R} d\lambda \delta(\mathcal{R} - \mathcal{R}_{\text{static}}, \lambda - 1) \Delta E(\mathcal{R}; T_{\text{el}}), \quad (7)$$

where, respectively, the “nonrelevant” temperature is set to zero, i.e.,  $T_{\text{el}} = 0$  K for  ${}^{\circ}F^{\text{ah}}$  and  $T_{\text{ion}} = 0$  K for  ${}^{\circ}F^{\text{el}}$ , and  $\delta$  is the Dirac delta function. The pure anharmonic free energy  ${}^{\circ}F^{\text{ah}}$  comes from atomic vibrations while the electronic temperature is kept fixed at 0 K, such that neither the forces nor the energies are affected by electronic excitations. The pure electronic free energy  ${}^{\circ}F^{\text{el}}$  is simply the electronic free energy of the ideal, static atomic structure (here corresponding to the bcc lattice) with coordinates  $\mathcal{R}_{\text{static}}$  and with the electronic temperature turned on.

For the coupling terms we write

$$F^{\text{el} \leftarrow \text{vib}}(T_{\text{ion}}, T_{\text{el}}) = \int d\mathcal{R} d\lambda \rho(\mathcal{R}; \lambda, T_{\text{ion}}, T_{\text{el}}=0) \Delta E(\mathcal{R}; T_{\text{el}}) - {}^{\circ}F^{\text{ah}} - {}^{\circ}F^{\text{el}}, \quad (8)$$

and

$$F^{\text{vib} \leftarrow \text{el}}(T_{\text{ion}}, T_{\text{el}}) = \int d\mathcal{R} d\lambda \rho(\mathcal{R}; \lambda, T_{\text{ion}}, T_{\text{el}}) \Delta E(\mathcal{R}; T_{\text{el}}) - F^{\text{el} \leftarrow \text{vib}} - {}^{\circ}F^{\text{ah}} - {}^{\circ}F^{\text{el}}. \quad (9)$$

Here,  $F^{\text{el} \leftarrow \text{vib}}$  is the change in the electronic free energy due to the ionic vibrations at the given temperature, which is reflected in a smoothening of the electronic density of states as the thermal displacements of atoms increase [37]. On the other hand,  $F^{\text{vib} \leftarrow \text{el}}$  is the effect of a temperature-consistent Fermi smearing on the forces that determine the configurational space distribution. Note here that the coupling terms are related to the full vibrational effects (not only the anharmonic ones), because we exclude all electronic temperature effects in the QH reference energies. With the above definitions, we have

$$\Delta F(T_{\text{ion}}, T_{\text{el}}) = {}^{\circ}F^{\text{ah}}(T_{\text{ion}}) + {}^{\circ}F^{\text{el}}(T_{\text{el}}) + F^{\text{el} \leftarrow \text{vib}}(T_{\text{ion}}, T_{\text{el}}) + F^{\text{vib} \leftarrow \text{el}}(T_{\text{ion}}, T_{\text{el}}). \quad (10)$$

In the direct-upsampling methodology [32], the pure anharmonic contribution  ${}^{\circ}F^{\text{ah}}$  is obtained via the following two steps: (1) Thermodynamic integration from the QH reference to the MTP ( $\Delta F^{\text{qh} \rightarrow \text{MTP}}$ ), and (2) upsampling to DFT ( $\Delta F^{\text{up}}$ ). During these two steps the electronic temperature is turned off. We thus have

$$F^{\text{ah}} = {}^{\circ}F^{\text{ah}} = \Delta F^{\text{qh} \rightarrow \text{MTP}} + \Delta F^{\text{up}}, \quad (11)$$

and, as indicated,  ${}^{\circ}F^{\text{ah}}$  directly corresponds to  $F^{\text{ah}}$  from Eq. (1). The remaining terms from the above discussion are captured within the direct-upsampling methodology via the last upsampling step for the electronic free energy using the FEP formula, i.e.,

$$F^{\text{el}} = -k_B T \ln \left\langle \exp \left( -\frac{E_{\text{el}}^{\text{DFT}} - E^{\text{DFT}}}{k_B T} \right) \right\rangle_{\text{MTP}}, \quad (12)$$

where  $k_B$  is the Boltzmann constant and  $E_{\text{el}}^{\text{DFT}}$  and  $E^{\text{DFT}}$  are the DFT energies including and excluding electronic

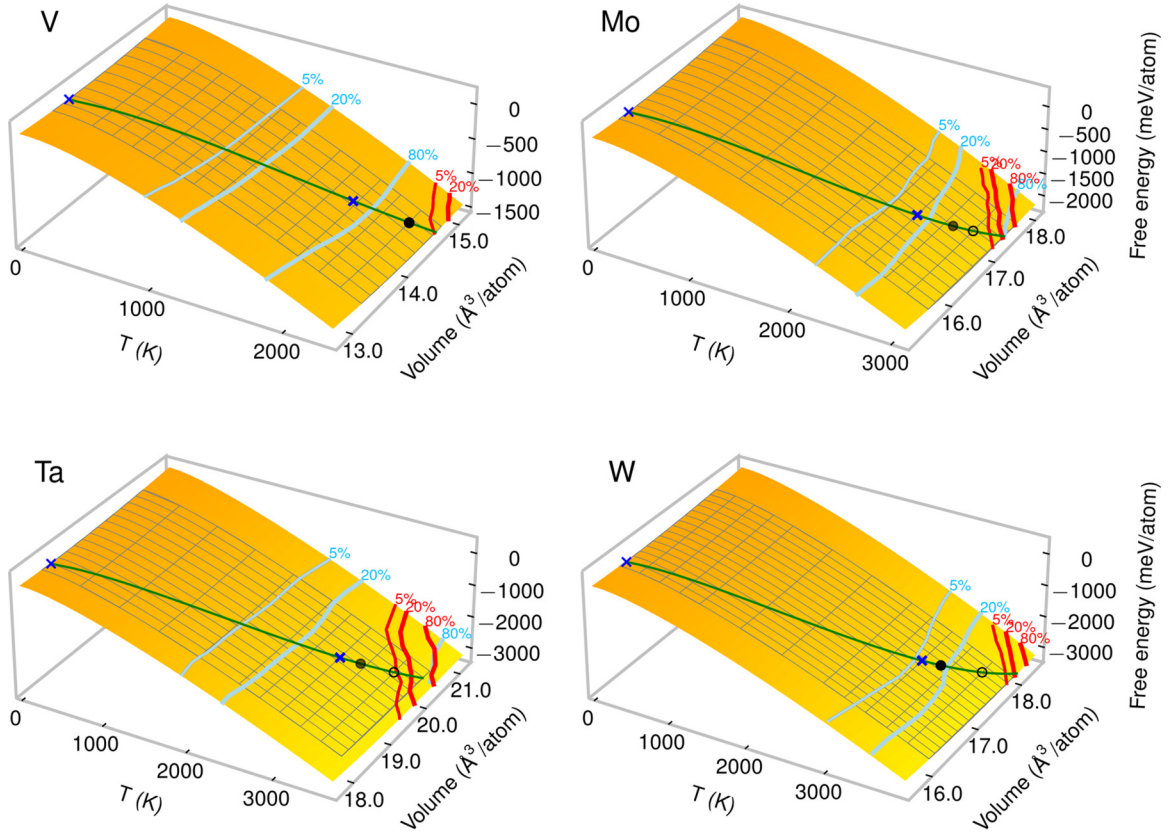


FIG. 1. Free-energy surfaces illustrating various quantities of relevance to the direct upsampling methodology: (1) the  $(V, T)$  grids by the crossings of the gray lines; (2) the probabilities for vacancy migration by the light blue contours; (3) the probabilities for Frenkel defect formation by the red contours; (4) the thermal expansions at ambient pressure by the green lines; (5) the experimental melting points by the hollow black circles; (6) the PBE-predicted melting points by the filled black circles (for Ta and Mo, these are estimates from our data); and (7) the explicitly computed  $G_{\text{vac}}^f$  values at 0 K and at  $(p^\times, T^\times)$  by the blue crosses. The probabilities of vacancy migration correspond to counts of the onset of migration in 3 ps long MTP MD runs. For Frenkel defects, the probabilities correspond to counts of formation in 10 ps long runs (in an ideal perfect bulk).

temperature, respectively. Thus, we can write

$$F^{\text{el}} = {}^\circ F^{\text{el}} + F^{\text{el} \leftarrow \text{vib}} + F^{\text{vib} \leftarrow \text{el}}, \quad (13)$$

where  $F^{\text{el}}$  corresponds to the definition in Eq. (1). The first-order approximation of the FEP formula in Eq. (12) gives  ${}^\circ F^{\text{el}} + F^{\text{el} \leftarrow \text{vib}}$ , and the higher-order terms account for  $F^{\text{vib} \leftarrow \text{el}}$ . Hence, each contribution to  $F^{\text{el}}$  can be separately calculated.

### B. Vacancy formation Gibbs energies

Computation of the full pressure and temperature dependence of the Gibbs energy of vacancy formation  $G_{\text{vac}}^f(p, T)$  is very demanding despite the effectiveness of the direct-upsampling methodology. One reason for this is that the error in  $G_{\text{vac}}^f$  scales with the number of atoms in the vacancy-containing supercell. Another reason is the tendency of the vacancy to migrate during the MD runs, which challenges a straightforward thermodynamic integration from the QH reference. In order to circumvent these difficulties, we take an approximate approach that reduces the computational effort significantly, yet captures the main physical mechanism: the strong (non-Arrhenius like) temperature dependence of  $G_{\text{vac}}^f$  due to anharmonic excitations [39,40].

Specifically, we first determine the perfect bulk free energy surfaces (Fig. 1) and the corresponding thermal expansion at ambient pressure (green lines). Next, we use the MTPs to perform a set of representative MD runs on supercells with a vacancy, to obtain information on the migration tendency of the vacancy. This tendency is indicated by the light blue lines in Fig. 1, which show the probability of the onset of migration of the vacancy. Based on this information we determine a point  $(V^\times, T^\times)$  on the perfect bulk thermal expansion line (thick blue crosses) that is high enough to capture the effect of temperature on  $G_{\text{vac}}^f(p, T)$ , but not too high (such as to cause vacancy migration) in order to allow for enough statistics during thermodynamic integration from the fixed-lattice QH reference. Typically, there is less than 60% probability of vacancy migration at the chosen  $(V^\times, T^\times)$ . We then apply direct upsampling to compute all free-energy contributions from Eq. (1) for the vacancy-containing supercell (with 53 atoms) at  $(V^\times, T^\times)$ . We obtain the Gibbs energy of the vacancy-containing supercell  $G(p^\times, T^\times)$  by performing a Legendre transformation. Here, we calculate the Gibbs energy also at ambient pressure, and approximate the volume in the vacancy-containing supercell with the volume of the perfect bulk  $V^\times$ . This amounts to neglecting the term related to the volume of vacancy formation. We note that the  $pV$  term at

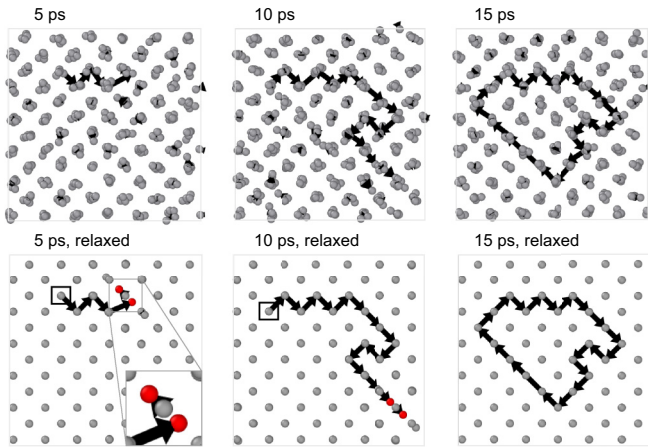


FIG. 2. Frenkel defect formation and kinetics in perfect bulk V during an MTP MD run at 2339 K. The top row shows MD snapshots and the bottom row the corresponding relaxed structures, seen along the [001] direction. The arrows indicate displacement vectors of the self-interstitial, which itself is shown by the red balls (dumbbell configuration), while the square indicates the vacancy that is left behind. After 15 ps of the self-interstitial formation, it comes back to the vacancy site and the defects annihilate.

ambient pressure is small; for example, 0.01 meV/atom for W with  $V^\times = 17.28 \text{ \AA}^3/\text{atom}$ , thus validating our approximation. Eventually, we are able to compute the Gibbs energy of vacancy formation  $G_{\text{vac}}^f(p^\times, T^\times)$  at the single point  $(p^\times, T^\times)$ .

In order to obtain the full temperature dependence of  $G_{\text{vac}}^f(p^\times, T)$ , we utilize the result of Ref. [39] where a quadratic temperature dependence was found to well describe the Gibbs energy of vacancy formation. Specifically, this dependence is given by

$$G_{\text{vac}}^f(p^\times, T) = H_{0\text{K}}^f + \frac{S'T^2}{2}, \quad (14)$$

where  $H_{0\text{K}}^f$  and  $S'$  are the two parameters to be determined. We determine  $H_{0\text{K}}^f$  by standard 0 K vacancy calculations (53-atom supercell) with relaxed atomic coordinates and at the 0 K equilibrium volume of the perfect bulk supercell (thus again neglecting the volume of formation term). The  $S'$  parameter is obtained by utilizing the  $G_{\text{vac}}^f(p^\times, T^\times)$  value from the previous paragraph.

### C. Frenkel defect formation

At very high temperatures and volumes, we have observed Frenkel defect formation [41,42] in the perfect bulk systems during the MTP MD runs. The probabilities of the defect formation are indicated in Fig. 1 by the red contour lines. Figure 2 illustrates the atomistic details of the Frenkel defect formation and kinetics at different MD times. At first, a self-interstitial is created leaving a vacancy behind. When relaxed, the self-interstitial is seen to form a “dumbbell” configuration with two atoms occupying a single lattice site (red balls). Both the vacancy and the self-interstitial migrate through the lattice, and it can happen that they annihilate after some time [43]. If such defects occur too frequently during the MD run, the convergence of the TI from a fixed-lattice QH reference becomes

inhibited. This is why it was not possible to obtain explicit free energy values at some of the highest  $(V, T)$  points, which explains the few missing points in the third column of Fig. 3 (e.g., for Ta at 3525 K).

### D. Computational details

For the DFT calculations, we used the projector-augmented wave (PAW) method [44] as implemented in the Vienna *ab initio* simulation package (VASP) [45,46]. We used PAW potentials with the semi-core p-electrons included in the valence band as provided in VASP 5.4.4. For W also the semi-core s-electrons were treated as valence electrons. For the XC functional, we used the generalized gradient approximation (GGA) in the PBE parametrization [35].

The finite-temperature DFT was realized with a temperature-consistent Fermi-Dirac distribution. For calculations excluding the electronic temperature, we instead used the first-order Methfessel-Paxton scheme [47] with a smearing width of 0.2 eV, with the energy extrapolated to zero smearing. The  $k$ -point meshes were constructed according to Monkhorst-Pack [48].

We used moment tensor potentials (MTPs) fitted with the MLIP code [33,49] as the intermediate, auxiliary potentials in the direct-upsampling procedure. The same MTPs were used for modeling both the perfect bulk and the vacancy-containing supercell, for each element.

The  $(V, T)$  grids used for the computation of the free energy surfaces contained  $9 \times 14$  (V),  $14 \times 15$  (Ta),  $12 \times 11$  (Mo), and  $16 \times 13$  (W) points. These grids are indicated by the gray lines in Fig. 1. Further details regarding direct up-sampling, including the DFT parameters, the MTPs and the effective QH references, can be found in the Supplemental Material [14].

## III. RESULTS AND DISCUSSION

### A. Free energies

Figure 3 shows the Gibbs energies  $G(T)$  at ambient pressure (first column), free energies  $F(V)$  at the experimental melting temperature (second column), and the complete anharmonic free-energy surfaces  $F^{\text{ah}}(V, T)$  as a projection onto the plane spanned by the volume and free-energy axes (third column) for the four bcc refractory systems.

On the total scale, the computed Gibbs energies including all finite temperature contributions (solid blue lines) follow closely the experiment-based CALPHAD-SGTE data [50] (open circles) for all elements. The zoom-ins to high temperatures provided in the insets reveal, however, deviations of a few tenths of meV/atom. For Ta, Mo, and W, the DFT PBE data are lower than the CALPHAD data. Such a behavior of the PBE functional was observed previously for other elements [32]. In contrast, the Gibbs energy for V is higher than the CALPHAD data at high temperatures, which is an unusual behavior for the PBE exchange-correlation functional. The difference in behavior can be correlated with the 0 K equilibrium lattice parameters. For Ta, Mo, and W, the calculated lattice parameter is larger than the experimental one, as seen in Table II. This is expected for PBE calculations [51]. For

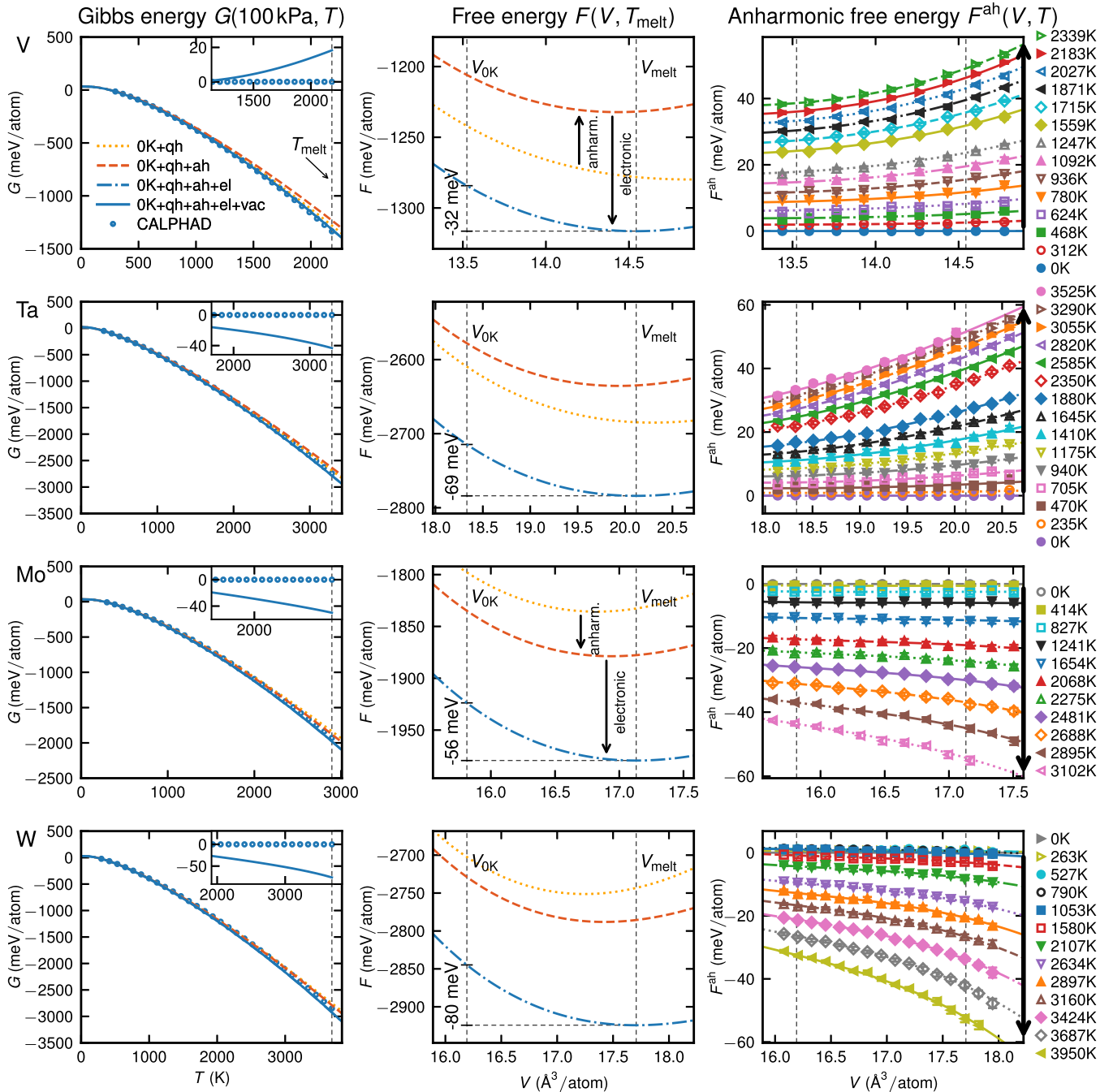


FIG. 3. *Ab initio* calculated Gibbs energy  $G(T)$  at 100 kPa, free energy  $F(V)$  at  $T_{\text{melt}}$ , and anharmonic free energy  $F^{\text{ah}}(V, T)$ , for the four elements using the PBE XC functional. The  $G(T)$  values are referenced to the minimum energy of the static lattice at 0 K. Results from CALPHAD-SGTE data [50] (aligned to the *ab initio* values at room temperature) are shown in blue dots for comparison. The insets contain the full *ab initio* Gibbs energy at high temperatures with respect to the CALPHAD-method values. For  $G(T)$  and  $F(V, T_{\text{melt}})$  curves including the contributions from 0 K, the effective QH potential (qh), anharmonicity (ah), and electronic temperature (el) are shown. The vacancy contribution (vac) is shown only for  $G(T)$  as it is only evaluated at  $V_p(T)$ .

$V$ , on the other hand, the PBE-predicted lattice parameter is slightly underestimated as also reported previously [51,52].

In the second column, the importance of the different contributions to the perfect bulk free energy becomes visible. As is characteristic for the high-melting refractory elements [37], the electronic contribution is large at the melting temperature for all four elements, lowering the free energy by more than  $-100$  meV/atom. The equilibrium volume at

the melting point (corresponding to the minimum of the curve) is slightly increased by the electronic contribution for all the elements. The anharmonic contribution seen as the difference between the orange and yellow lines for the melting temperature in the second column, or explicitly for all temperatures in the third column, is likewise relatively large for these bcc refractory systems. The magnitude of the anharmonic free energy goes up to about 60 meV/atom,

TABLE II. PBE-predicted and experimental lattice parameters and melting points for the systems.

	$a_{0K}^{\text{PBE}}$ (Å)	$a_{0K}^{\text{exp}}$ (Å)	$T_{\text{melt}}^{\text{PBE}}$ (K)	$T_{\text{melt}}^{\text{exp}}$ (K)
V	2.998	3.024 <sup>a</sup>	2154 <sup>b</sup>	2183 <sup>c</sup>
Ta	3.320	3.299 <sup>a</sup>	3000 <sup>d</sup>	3290 <sup>c</sup>
Mo	3.160	3.141 <sup>a</sup>	2750 <sup>d</sup>	2895 <sup>c</sup>
W	3.186	3.160 <sup>a</sup>	3330 <sup>b</sup>	3687 <sup>c</sup>

<sup>a</sup>Recited from Ref. [51]<sup>b</sup>From Ref. [53].<sup>c</sup>From Ref. [54].<sup>d</sup>Estimated based on fit to the CALPHAD [50] heat capacity.

which is significantly larger than the magnitude observed previously for fcc systems [8]. A qualitative difference is seen in the anharmonic free energy between the group 5 and group 6 elements. The group 5 elements V and Ta both have a positive anharmonic free-energy contribution. This is similar to the values obtained for the other group 5 element Nb [32]. Contrarily, the group 6 elements Mo and W have a large and negative anharmonic free-energy contribution. This difference in trend has recently been explained in terms of opposite effects of the renormalization of phonons on the electronic density of states (eDOS) and force constants in group 5 and group 6 elements, respectively [9].

The dense  $(V, T)$  grids for  $F^{\text{ah}}$  shown in the third column of Fig. 3 are a prerequisite for obtaining converged thermodynamic properties, which rely on derivatives of the free-energy surface. It is also important that the grids extend beyond the volume range of interest ( $V_{0K}$  to  $V_{\text{melt}}$ ) and above the highest target temperature (here experimental melting points). A sufficiently high-order polynomial is needed to capture the  $V$  and  $T$  dependence of the thermodynamic properties, and this polynomial requires a sufficiently dense and extended  $(V, T)$  grid to avoid overfitting.

Based on the approach taken to compute the impact of thermal vacancies (Sec. II B), we have the full temperature-dependent contribution to  $G(T)$  at ambient pressure available. This contribution corresponds to the difference between blue-dashed and blue lines in the first column of Fig. 3. However, it is not recognizable due its extremely small value at all temperatures, which is below 1 meV/atom even at the melting point for any of the elements.

### B. Thermodynamic properties

Figure 4 shows the calculated heat capacity, linear thermal expansion coefficient, and bulk modulus for the four systems. The electronic and the anharmonic contributions play an important role in the final, predicted properties, as they significantly alter the outcome of the QH approximation. The electronic contribution affects thermodynamic properties similarly in all the four elements, i.e., it increases the heat capacity and the expansion coefficient and decreases the bulk modulus (change from red dashed to blue dash-dotted lines). Contrarily, the opposite sign of the anharmonic free energy in the group 5 and group 6 elements (discussed in the previous section) affects the thermodynamic properties in opposite

ways. For example, the expansion coefficient decreases in V and Ta, as compared to Mo and W, when including the anharmonic vibrations (change from yellow dotted to red dashed lines). The vacancy contribution is almost negligible in the thermodynamic properties (solid blue and dashed blue lines fall almost on top of one another), with only a small effect seen in the heat capacity very close to the melting point.

The solid blue curves include all contributions to the free energy. For Ta, Mo, and W, the heat capacity and expansion coefficient are overestimated in comparison to CALPHAD and experimental data, and the bulk modulus for Mo and W is underestimated. The trend is opposite for V. This can again be correlated with the difference in the predicted lattice parameters inherent to the GGA-PBE functional, in comparison to experimental values. Ta, Mo, and W show a softening as expected by the overestimated lattice parameter, while V is correspondingly stiffer.

Even though the agreement with experimental data is satisfactory, there are still discrepancies between the PBE-predicted properties including all contributions and the experimental values, especially as the temperature nears the experimental melting point. We foresee this as an inherent error in the *ab initio*-predicted values coming from the XC functional. To compensate for the discrepancy, one possible approach would be to calibrate the thermodynamic properties by utilizing the experimental 0 K equilibrium lattice parameters and bulk moduli [65]. However, since we are mainly interested in the accuracy of the thermodynamic properties at high temperatures and since we prefer a self-contained theoretical approach, we propose to rescale the temperature dependence of the properties with the melting temperature, as described next.

### C. Properties on the homologous temperature scale

Figure 5 shows the calculated thermodynamic properties including all contributions on the homologous temperature scale. The homologous temperature scale uses a relative temperature normalized with respect to a *consistent* melting temperature. For the experimental and CALPHAD data, the experimental melting points as given in Table II are used to rescale the temperature axis. For the *ab initio* results, for V and W, the *ab initio*-predicted PBE melting points are used instead for the rescaling. The PBE melting points were calculated using the TOR-TILD approach [53,66] and are listed in Table II. The TOR-TILD calculations have so far been performed only for unary V and W.

The agreement with experiments for V and W is remarkable on the homologous temperature scale. For Ta and Mo, we rely on the excellent agreement seen for V and W, and estimate the PBE melting temperatures by rescaling the PBE heat capacities to match the CALPHAD ones. Our estimates agree very well with recent predictions of the PBE melting temperature using machine-learning interatomic potentials [67]. We then use our estimated melting points to obtain the homologous temperature scale for Ta and Mo. In the third column in Fig. 5, instead of the absolute bulk modulus, we plot the relative bulk modulus with respect to its corresponding 0 K value on the homologous temperature scale, to achieve a similar relative comparison.

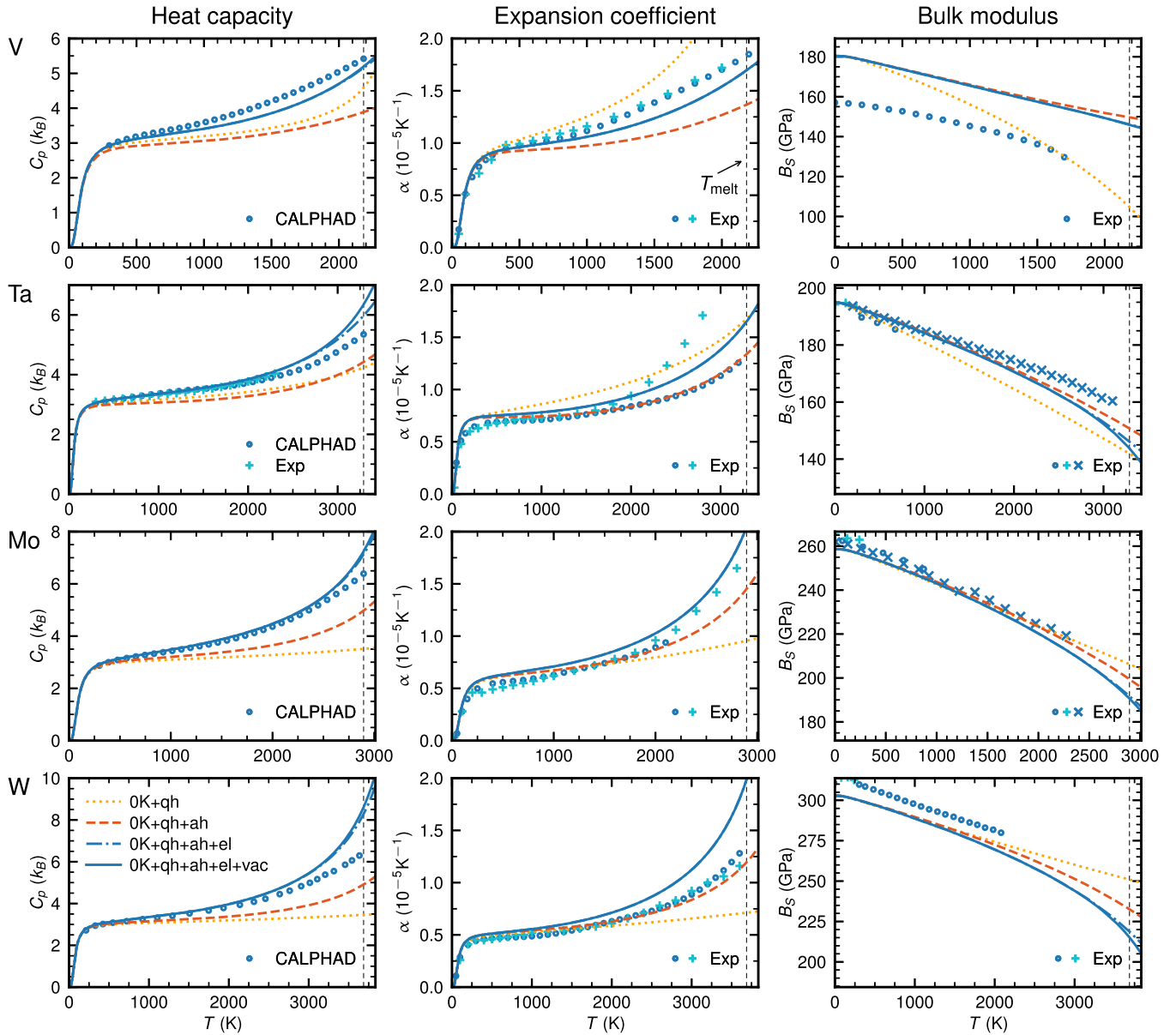


FIG. 4. *Ab initio* calculated  $C_p(T)$ ,  $\alpha(T)$ , and  $B_S(T)$  up to the melting point for V, Ta, Mo, and W at ambient pressure. Calculations are compared to CALPHAD or experimental results shown in blue symbols. Results considering different excitation mechanisms [effective QH (qh), including anharmonic (ah), electronic (el), and from vacancies (vac)] are shown. The following CALPHAD or experimental references are used for comparison:  $C_p$  [50] and [55] (Ta);  $\alpha(T)$  [56,57]; and  $B_S(T)$  [58] and [59] (V), [60,61] (Ta), [62,63] (Mo), and [64] (W).

On the homologous temperature scale, the differences seen between the *ab initio* values and the experimental values in Fig. 4 are redeemed to a large extent. The agreement between the *ab initio*-predicted properties and the experimental ones is much stronger on the homologous scale. The changes in the thermodynamic plots on the homologous temperature scale are less evident for V compared to the other elements. This is because the predicted melting point for V estimated by the PBE functional is very close to the experimental one. Hence, the results remain almost the same as on the absolute temperature scale. Therefore the PBE results for V still slightly underestimate the heat capacity and thermal expansion coefficient compared to the experimental data. This discrepancy may be related to a missing paramagnetic contribution, the determination of which is beyond the scope of our paper. We

further note that the temperature dependence of the relative bulk moduli (third column in Fig. 5) is in excellent agreement with the experimental data for all elements.

The overall outstanding agreement of our results to experimental data on the homologous temperature scale warrants the use of the *ab initio* data to evaluate and resolve experimental discrepancies. For example, this can be illustrated using the expansion coefficient of Ta in Fig. 5. The *ab initio* results fall almost on top of one set of experimental data (represented by blue circles), whereas the other set of data (light blue plus marks) diverge above  $0.5 T/T_m$ . Given the overall reliability of our data, we can say with good conviction that the second set of experimental data is inaccurate, either coming from challenging experimental conditions at high temperature, or from approximations in the measurement.

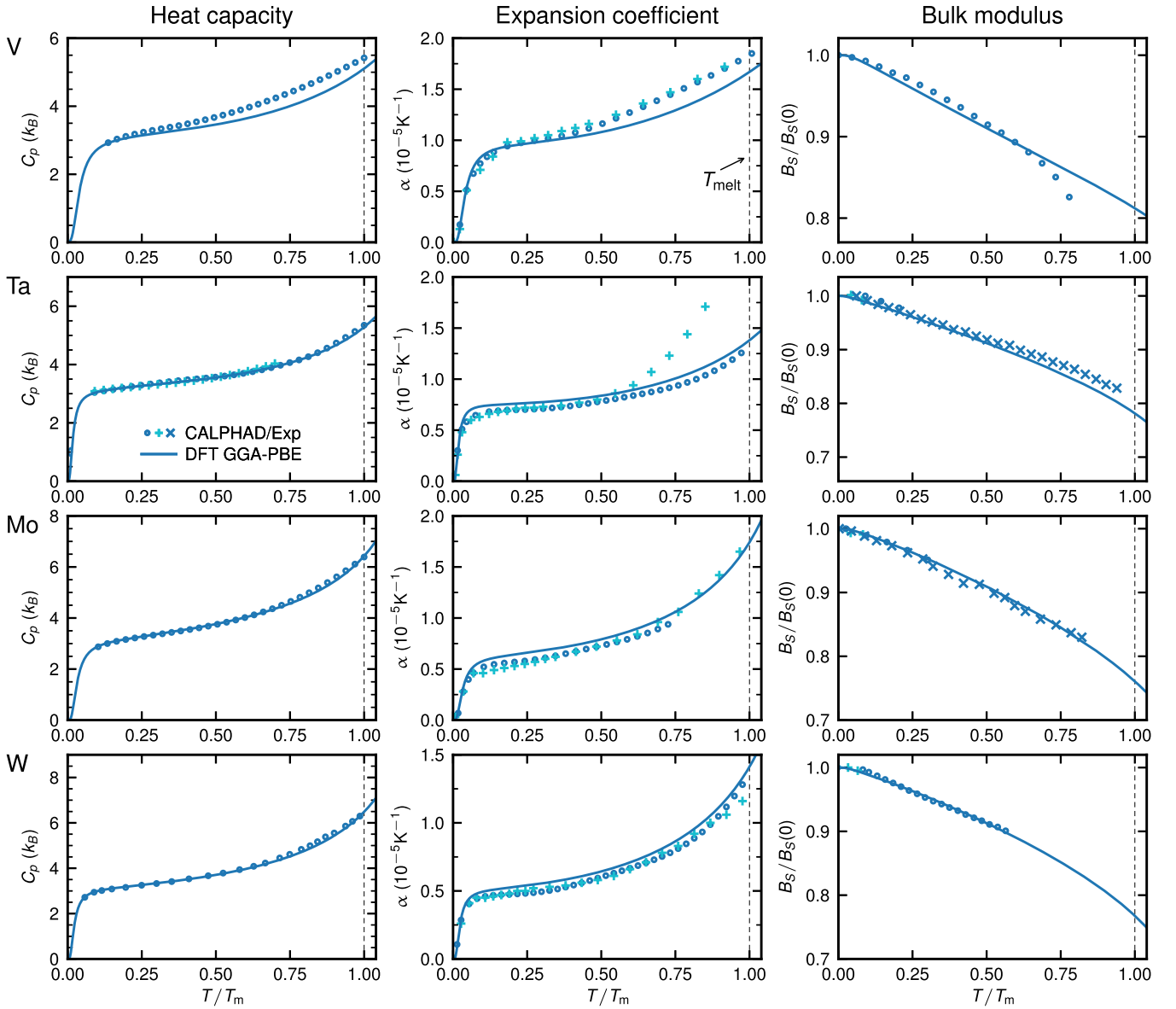


FIG. 5. *Ab initio* calculated  $C_p(T)$ ,  $\alpha(T)$ , and  $B_S(T)/B_S(0)$  including all contributions on a homologous temperature scale, compared to CALPHAD/experimental data [50,55–64]. The melting points used for the homologous scale are (1) PBE-predicted values for *ab initio* V and W, (2) estimated values for *ab initio* Ta and Mo based on rescaling to the corresponding CALPHAD heat capacities, and (3) experimental values for CALPHAD/experimental data. The melting temperatures used are specified in Table II. The third column is the relative bulk modulus, where  $B_S(0)$  is the corresponding 0 K value.

#### D. Gibbs energies of vacancy formation

We have shown that the effect of thermal vacancies on the Gibbs energy, and eventually to the thermodynamic properties of the bulk, is very small and almost negligible. Nevertheless, calculating the temperature-dependent vacancy formation Gibbs energy  $G_{\text{vac}}^f(p, T)$  is crucial in studying vacancy diffusion, which is relevant, e.g., for phase transformations. The procedure to obtain  $G_{\text{vac}}^f(p, T)$  was outlined in Sec. II B. As a first step, we calculate the 0 K enthalpy of vacancy formation  $H_{\text{vac}}^f$ .

Table III shows a list of previously calculated  $H_{\text{vac}}^f$  values from literature [and one high-temperature  $G_{\text{vac}}^f(T)$ ]. Evidently, there is scatter in the existing literature data,

originating from different XC's, methodologies and approximations used for the calculations. Likewise, experimental values (not shown here) determined from positron annihilation spectroscopy or resistivity measurements possess large uncertainties that range at least several hundreds of meV/vacancy [72]. This is because Arrhenius-type temperature dependencies are fit to high-temperature experimental data, and the model does not extrapolate well to 0 K [39].

In the penultimate row in Table III, we show our currently calculated values of  $H_{\text{vac}}^f$ , determined to high accuracy within the PBE XC functional. Additionally, in the last row in the table, we also show the Gibbs energy of formation  $G_{\text{vac}}^f$  at  $(p^\times, T^\times)$  [see Sec. II B for how  $(p^\times, T^\times)$  is chosen]. Using the  $H_{\text{vac}}^f$  value at 0 K and the  $G_{\text{vac}}^f$  value at

TABLE III. Vacancy formation enthalpies ( $H_{\text{vac}}^f$ ) at 0 K and Gibbs energies ( $G_{\text{vac}}^f$ ) at finite temperatures in eV/vacancy. For the finite-temperature results of this paper, also the bounds for the 95% confidence intervals resulting from the thermal averaging in the direct-upsampling procedure are presented. All of the used abbreviations are expanded in the Supplemental Material [14].

Ref.	Method	XC		$T$	V	Ta	Mo	W
[68]	FP-LMTO	LDA	unrelaxed	0 K	3.06	3.49	3.13	3.27
[69]	FP-LMTO	LDA	unrelaxed	0 K	2.20	2.41	2.50	3.04
[70]	NC	LDA		0 K	2.48	3.20	2.85	3.35
[70]	FP-LMTO/NC	LDA		0 K	2.65	3.20	3.00	3.64
[70]	FP-LMTO/NC	PW91		0 K	2.55	3.20	2.90	3.60
[41]	PAW	PBE		0 K	2.04	2.86	2.79	3.22
[41]	PAW	AM05		0 K	2.61	3.17	3.11	3.62
[71]	PAW	AM05		2481 K			2.51 <sup>a</sup>	
This paper	PAW	PBE		0 K	2.42	2.91	2.84	3.36
This paper	PAW	PBE		70–85% $T_{\text{melt}}$	$2.04 \pm 0.06$	$2.35 \pm 0.08$	$2.15 \pm 0.07$	$2.42 \pm 0.06$

<sup>a</sup>Estimated from the temperature dependent energy of formation in their results.

( $p^\times, T^\times$ ) in Eq. (14), we obtain  $S'$  and thus the temperature dependence of the Gibbs energy of vacancy formation  $G_{\text{vac}}^f(p, T)$ .

Figure 6 shows the such-obtained Gibbs energies of vacancy formation on the absolute and the homologous temperature scales. The points used to determine the quadratic temperature dependencies according to Eq. (14) are represented with cross marks. For comparison, in Fig. 6(a), we also show the Gibbs energy of vacancy formation for three fcc systems (Al, Cu, and Ni) from previous studies [39,40].

A strong deviation from an Arrhenius-type temperature dependence of the Gibbs energy of vacancy formation was proven earlier for the fcc systems. A linear model was unable to simultaneously capture both high-temperature experimental Gibbs energies, and computed 0 K vacancy formation enthalpies. A quadratic temperature dependence was thus formalized in Ref. [39]. The breakdown of the Arrhenius-type behavior was shown to arise from explicit anharmonic behavior, especially seen in the direction from the nearest neighbor towards the center of the vacancy in the fcc systems. In the bcc refractories, with a much stronger anharmonicity, it thus becomes necessary to use such a quadratic behavior of the vacancy formation Gibbs energy.

The  $S'$  parameter that quantifies the temperature dependence in Eq. (14) falls in a similar range between 0.0018 and  $0.0036 k_B \text{K}^{-1}$  for both the previously calculated fcc unaries and the current bcc refractories. Since we use the same quadratic formulation, the temperature dependence of  $G_{\text{vac}}^f$  [Fig. 6(a)] is also similar in the bcc refractories to the fcc systems, but 2–3 times higher in magnitude. The temperature-dependent vacancy concentration for the bcc refractories is also calculated from  $G_{\text{vac}}^f(p, T)$ , and is shown in the inset to Fig. 6(b). At  $T_m$ , the vacancy concentration lies between  $10^{-3}$  and  $10^{-4}$  vacancies per atom, which is in the same order of magnitude as typical experimental values [72].

### E. Electron-vibration coupling

The strong contribution of the electronic free energy has been highlighted for all four refractory systems in the second column of Fig. 3 (difference between red and blue lines). The electronic free energy can be decomposed into “pure” and “coupling” contributions, where the coupling includes both the effect of thermal vibrations on the electronic free energy  $F^{\text{el} \leftarrow \text{vib}}$ , and the electronic temperature on the atomic forces  $F^{\text{vib} \leftarrow \text{el}}$ . Each of these terms was individually defined in Sec. II A. Here, we separately analyze their contribution to

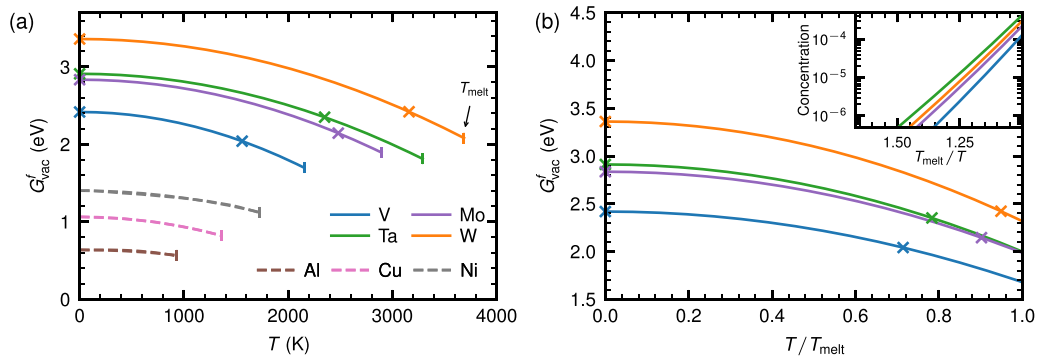


FIG. 6. Calculated vacancy formation Gibbs energies (a) on an absolute temperature scale compared to fcc elements from Refs. [39,40] up to the experimental melting points, and (b) on the homologous temperature scale relative to the PBE-predicted melting temperature. The crosses represent the calculated data points and the lines are the temperature dependencies using Eq. (14). The inset in (b) shows the corresponding vacancy concentrations.

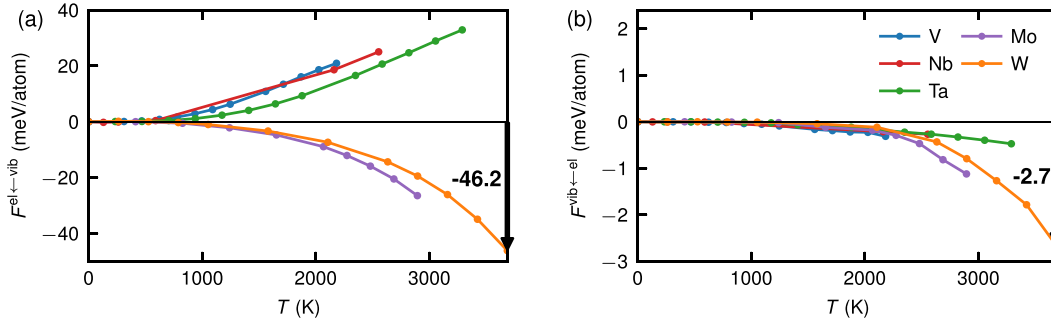


FIG. 7. Temperature dependence of the coupling contributions to the free energy at ambient pressure for the bcc refractory systems, including Nb data from Ref. [32]. (a)  $F^{\text{el}\leftarrow\text{vib}}$ ; the difference between the electronic contribution calculated from configurations with ionic temperature and that from the ideal 0 K lattice. (b)  $F^{\text{vib}\leftarrow\text{el}}$ ; the effect on the vibrational free energy, from using finite-temperature DFT ( $T_{\text{el}} = T_{\text{ion}}$ ) as compared to the Methfessel-Paxton smearing scheme ( $T_{\text{el}} = 0$  K).

the above-mentioned strong, total electronic free energy [ $F^{\text{el}}$  in Eq. (13)] for the four refractory metals in focus so far, and additionally for bcc Nb.

Figure 7(a) shows  $F^{\text{el}\leftarrow\text{vib}}(T)$ . The contribution of  $F^{\text{el}\leftarrow\text{vib}}$  was already calculated for Nb and W in Ref. [37]. Having calculated the results here for more refractory elements, we can infer that there are two classes with either a strong increase (V, Nb, Ta) or a strong decrease (Mo, W) of  $F^{\text{el}\leftarrow\text{vib}}(T)$  with temperature. These two classes reflect the group structure of the periodic table. The elements with increasing  $F^{\text{el}\leftarrow\text{vib}}(T)$  belong to the group 5 elements, and the ones with a decreasing  $F^{\text{el}\leftarrow\text{vib}}(T)$  to the group 6 elements. Interestingly, on an absolute temperature scale as utilized in Fig. 7(a), we observe a rather similar temperature dependence of the magnitude of  $F^{\text{el}\leftarrow\text{vib}}(T)$  for all five elements. The strongest contribution of  $\approx -46$  meV/atom is observed for W at its melting point.

The difference in trends in  $F^{\text{el}\leftarrow\text{vib}}$  [Fig. 7(a)] can be explained in light of recent discussions [9,37]. We take Ta (group 5) and W (group 6) as examples. Figure 8 shows the impact of temperature on their eDOS'. The blue curves show the eDOS for the static, ideal bcc lattice and the black dashed curves are the average eDOS' for snapshots from an MD run at  $T^{\text{melt}}$  (excluding the impact of electronic temperature). The Fermi level in Ta lies close to a peak in the static eDOS, whereas in W it lies in a valley. The eDOS' are significantly flattened due to thermal vibrations, as seen by the black dashed curves. In Ta, this lowers the value of the eDOS at the Fermi level, leading to a decrease in magnitude in  $F^{\text{el}}$  and thus to a positive  $F^{\text{el}\leftarrow\text{vib}}$ . In W, on the other hand, thermal vibrations increase the eDOS at the Fermi level, thereby increasing the magnitude of  $F^{\text{el}}$  (i.e., negative  $F^{\text{el}\leftarrow\text{vib}}$ ).

Including also electronic temperature by applying the Fermi-Dirac distribution in the self-consistent DFT calculations has a negligible impact on the eDOS', as seen by comparing the orange curves to the black dashed ones in Fig. 8. Nevertheless, there is an influence of the electronic temperature on the free energy. This effect is described by  $F^{\text{vib}\leftarrow\text{el}}(T)$ , which we show in Fig. 7(b). The  $F^{\text{vib}\leftarrow\text{el}}$  contribution is calculated from the higher-order terms of the FEP formula [Eq. (12)] on snapshots generated by the MTP. As can be observed, it is significantly smaller than  $F^{\text{el}\leftarrow\text{vib}}$ , and negative for all the bcc refractory systems. Only in the case of W, near its melting point, does the contribution reach

an appreciable magnitude of  $-2.7$  meV/atom. Since the contribution is evaluated from the higher-order terms of the FEP formula, this contribution will by definition always be negative.

To understand the effect of  $T_{\text{el}}$  on the vibrations in the refractory systems, we first analyze the impact of  $T_{\text{el}}$  on MD forces. Figure 9 shows the correlation between forces computed with the Methfessel-Paxton smearing and forces resulting from Fermi-broadened self-consistent calculations for the same snapshots. We see a good correlation with small standard deviations for all refractory metals. A slight increase of the standard deviation is observed for the heavier elements

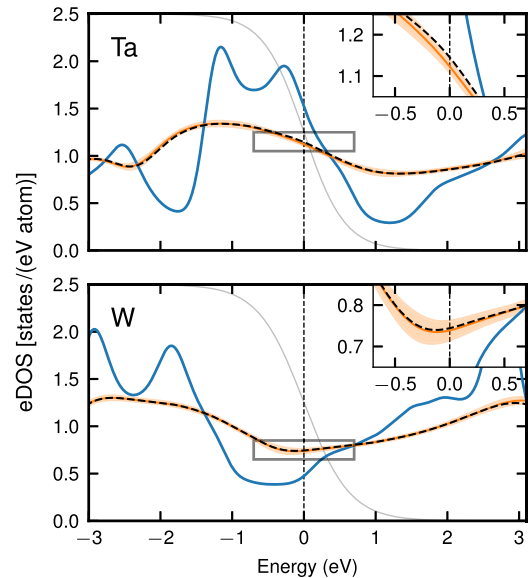


FIG. 8. Electronic density of states (eDOS) for Ta and W as a function of energy relative to the Fermi level. The blue curves correspond to the 0 K ideal bulk, and the black dashed and the orange curves correspond to the average from randomly chosen snapshots at  $T_{\text{melt}}$  excluding and including the electronic temperature, respectively. The standard deviation is marked by the orange shaded area. The insets show detailed views around the Fermi level, which are of relevance to the convergence properties discussed in the Supplemental Material [14]. The solid gray lines indicate the Fermi broadening of the electronic occupancies at the melting temperature.

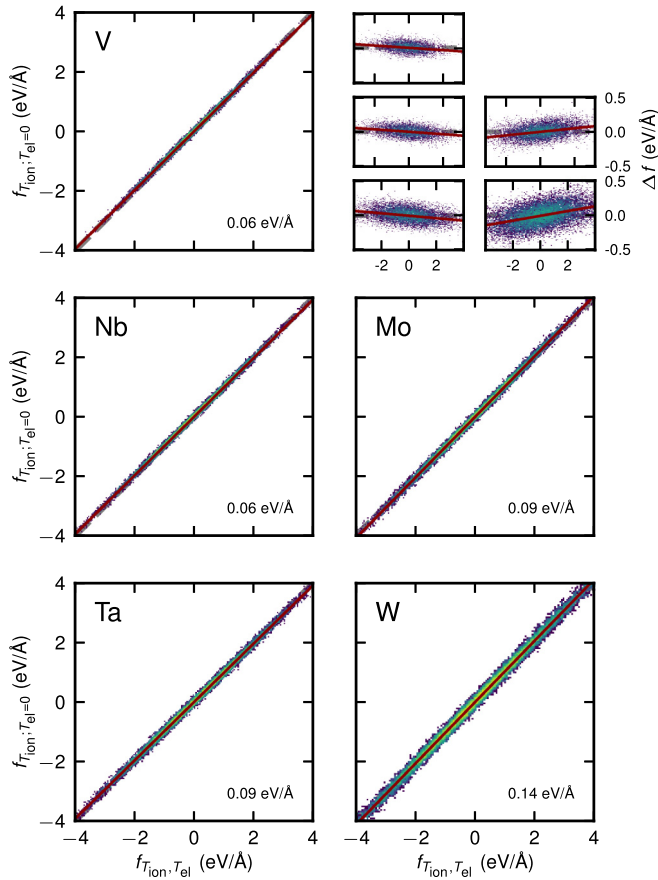


FIG. 9. Correlation between forces with ( $f_{T_{ion}, T_{el}}$ ), and without ( $f_{T_{ion}, T_{el}=0}$ ) the impact of electronic temperature  $T_{el}$ . The top right corner shows the corresponding difference in forces ( $f_{T_{ion}, T_{el}=0} - f_{T_{ion}, T_{el}}$ ). The red lines are trend lines (linear fits) to guide the eye and the root-mean-square difference is denoted in the lower right corners. Note that the configurations are generated without electronic temperature.

and for the group 6 elements. This trend is better visible in the smaller plots in the top right part of the figure, where the difference in forces (without and with electronic temperature) is plotted. The difference plots reveal another interesting feature that is highlighted by the red lines, which reflect linear fits to the data. For V, Nb, and Ta (group 5), when including  $T_{el}$  the average forces become slightly stiffer (negative slopes for the red lines). This can also be explained by comparing the dashed black and orange lines in the insets in Fig. 8. For Ta (and for group 5 elements), the effective decrease in the eDOS due to the partial occupancy around the Fermi level, where the slope is negative (see Fig. 8), leads to an increased relative stability of the structure. In contrast, the electronic temperature occupancy for Mo and W (group 6) leads to an effective increase in the eDOS around the Fermi level (where the slope is positive), and gives instead softer forces (positive slope for the red lines in Fig. 9).

The effect of  $T_{el}$  on the atomic vibrations is further unveiled by analyzing the nearest-neighbor distributions during MD simulations with and without the electronic temperature. We demonstrate this for W in Fig. 10. The first row shows (a) the first-nearest-neighbor (1NN) and (b) the second-nearest-

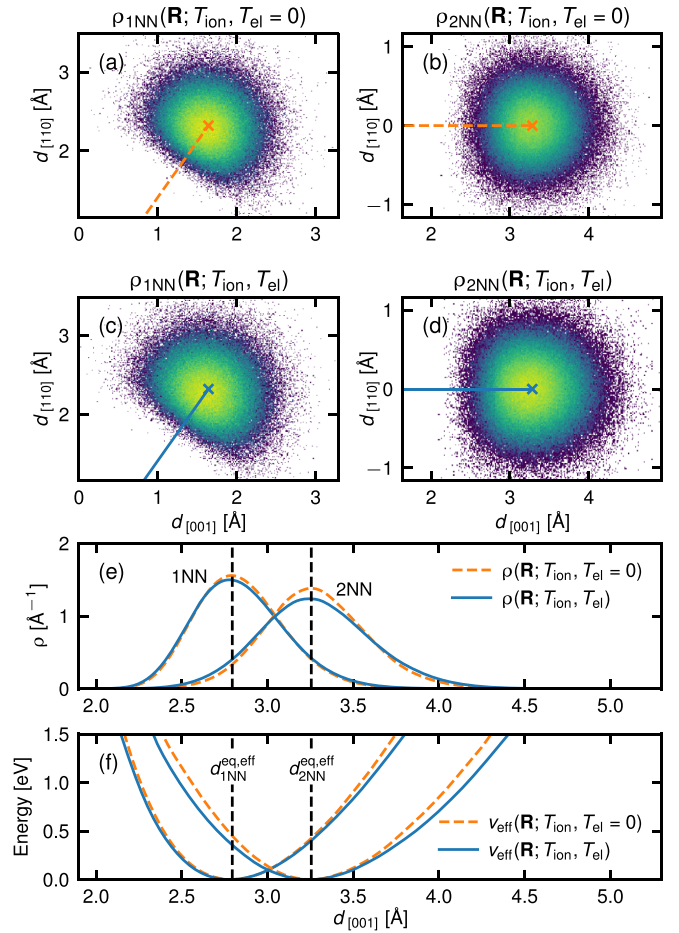


FIG. 10. Distribution density histograms of first [(a),(b)], and second [(c),(d)] nearest-neighbor (1NN and 2NN) distances projected onto the  $(\bar{1}10)$  plane for W at  $T_{melt}$  and close to  $V_{melt}$  without Fermi smearing [(a),(c)] and with Fermi smearing [(b),(d)]. (e) Distribution densities,  $\rho$ , corresponding to (a, b, c and d) with applied Gaussian smearing with standard deviation  $0.05 \text{ \AA}$ . They are projected onto the  $[111]$  and  $[001]$  vector, for 1NN and 2NN, respectively. (f) Effective 1D potentials,  $v_{eff}$ , constructed from the distribution densities. For Ta the effect is smaller, see Fig. S4 in the Supplemental Material [14].

neighbor (2NN) distribution contours projected on the  $(\bar{1}10)$  plane during an MTP MD run at  $T_{melt}$  with  $T_{el} = 0 \text{ K}$ . The corresponding contours in the second row [(c) and (d)] are from an MD run with an MTP trained to DFT that includes the electronic temperature. In the 2D contour plots no differences are visible. Thus we additionally plot the 1D distribution densities and the corresponding effective 1D potential ( $v_{eff} = -k_B T \ln \rho$ ) in (e) and (f) for the 1NN and 2NN, respectively. When  $T_{el}$  is included, the softer forces seen for W (see also Fig. 9) lead to a broader distribution (solid blue curves), which is slightly more apparent in the 2NNs. In Ta (group 5), there is almost no visible effect of  $T_{el}$  on the distributions (cf. Fig. S4 in the Supplemental Material [14]), which is consistent with the much smaller impact of  $T_{el}$  on the forces seen in Fig. 9 and the smaller  $F^{vib \leftarrow el}(T)$  values in Fig. 7(b).

It should be stressed that, although there is a small difference in trend in the atomic forces while including  $T_{el}$  between

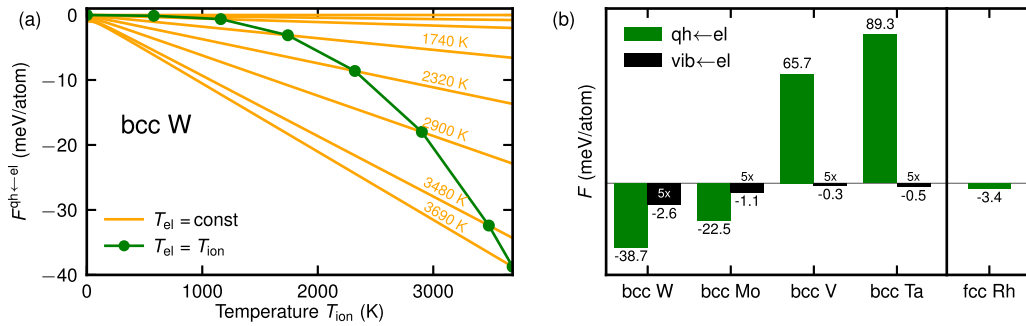


FIG. 11. (a) Difference in the QH vibrational free energy for bcc W at constant volume as a function of ionic temperature  $T_{\text{ion}}$  for different electronic temperatures  $T_{\text{el}}$ . The difference is with respect to the QH free energy at  $T_{\text{el}} = 0$  K. The orange lines correspond to several different, fixed  $T_{\text{el}}$  and the green line to  $T_{\text{el}} = T_{\text{ion}}$ . (b) Difference in the QH vibrational free energy at  $T_{\text{melt}}$  and close to  $V_{\text{melt}}$  (green bars) for all four elements and additionally for fcc Rh [73], compared to  $F^{\text{vib}←\text{el}}$  (black bars). The black bars are scaled with a factor of five for visibility. The absolute values are denoted at the edge of each bar.

group 5 and group 6 refractories, there is always a *decrease* in  $F^{\text{el}}$ . That is, when the *correct* forces corresponding to the energies are taken into account, the free energy will always decrease, in consistency with the higher-order terms of the FEP always being negative.

#### F. Exaggerated impact of electronic temperature in the quasiharmonic approximation

Based on the accurate  $F^{\text{vib}←\text{el}}$  data [Fig. 7(b)], we can evaluate the possibility to approximate this term by its QH counterpart, analogously labeled  $F^{\text{qh}←\text{el}}$ . We determine  $F^{\text{qh}←\text{el}}$  by varying the electronic temperature (up to the melting point) in the calculation of the forces from which the dynamical matrix is derived. The forces correspond to snapshots from a 20-K MD run according to the standard procedure within the direct-upsampling methodology. Defined in this way,  $F^{\text{qh}←\text{el}}$  captures the impact of electronic temperature on the low-temperature-QH free energy.

Figure 11(a) shows a detailed analysis of the  $F^{\text{qh}←\text{el}}$  contribution for W. The orange lines correspond to the change in the QH free energy for different fixed electronic temperatures  $T_{\text{el}}$  (indicated by the orange numbers). The green line shows the change in the QH free energy as the electronic temperature changes correspondingly with the ionic temperature ( $T_{\text{el}} = T_{\text{ion}}$ ). As  $T_{\text{el}}$  increases, the QH free energy becomes more and more negative. This means that the electronic temperature has a softening effect on the forces and the dynamical matrix in W. When  $T_{\text{el}} = T_{\text{melt}}$ , the impact is strongest and almost amounts to  $-40$  meV/atom. This  $F^{\text{qh}←\text{el}}$  value is more than an order of magnitude more negative than the more accurate  $F^{\text{vib}←\text{el}}$  value of  $-2.6$  meV/atom for bcc W. Similarly exaggerated  $F^{\text{qh}←\text{el}}$  values at  $T_{\text{melt}}$  are found also for bcc Mo, V, and Ta as displayed in Fig. 11(b). The exaggerated  $F^{\text{qh}←\text{el}}$  values can be negative as seen for W and Mo, or positive as for V and Ta, but in any case, they deviate from the physically more relevant  $F^{\text{vib}←\text{el}}$  values.

We note that the strong impact of the electronic temperature on the low-temperature-QH free energy may be a feature of the present bcc refractory systems. A previous study [73] showed a much smaller impact for fcc Rh, in the range of a

few meV/atom as indicated in Fig. 11(b). In another study [74], it was found that the impact is negligible also for hcp Fe.

#### IV. CONCLUSIONS

The key finding in this paper is the exceptional agreement of the thermodynamic properties with experimental data on the homologous temperature scale. By plotting on such a self-consistent scale, it is possible to remove the main shortcoming of the exchange correlation (XC) functional. The resulting strong agreement with experimental data provides confidence in the predictive power of density-functional theory, even when using the traditionally underbinding PBE XC functional. In particular, our finding suggests that the deficiency of the PBE functional is confined to an overall underestimation of the bond strength, while higher-order interactions and correlation functions—responsible for the detailed temperature dependencies of the thermodynamic properties—are very well described as compared to experiment. Preliminary calculations indicate that these findings extend to the LDA functional as well. The agreement with experimental data puts us in a position to use the *ab initio* results to evaluate ambiguities in experimental measurements of heat capacities and expansion coefficients, which are especially difficult to measure at near-melting temperatures. We can also confidently predict highly accurate thermodynamic properties for various systems in regions where it is difficult or not possible to perform experiments.

For example, direct upsampling was previously applied to a refractory TaVCrW HEA, to predict properties up to DFT accuracy [31], but was not validated due to the lack of experimental data. In an ongoing work [53], the melting point of the TaVCrW alloy is being calculated, also to *ab initio* accuracy. By using the predicted melting point, we will be able to plot the previously calculated thermodynamic properties on a corresponding homologous temperature scale. The results could then be used to ascertain high-temperature experimental measurements of the TaVCrW alloy in the future.

In order to achieve such superior accuracy in thermodynamic properties, two crucial points need to be kept in mind: (1) A dense sampling of the free-energy surface to obtain

highly-converged derivatives, and (2) inclusion of all relevant free-energy contributions. Both of the above are achieved with the direct-upsampling methodology. Anharmonic free energies contribute up to 60 meV/atom in magnitude in the bcc refractories, which is much larger than for fcc elements. Different trends between the group 5 and group 6 elements are observed in the anharmonic behavior, which have been explained by comparing the static and high-temperature electronic density of states.

We have also derived explicit expressions for the temperature-dependent coupling between electronic and atomic vibrations. The effect of vibrations on the electronic free energy is quite strong in bcc refractories, in the range of several tens of meV/atom. Once again, there is a group trend (different in group 5 and group 6) in the direction in which the electronic free energy changes. On the other hand, the effect of electronic temperature on the vibrational free energy is smaller by an order of magnitude ( $<3$  meV/atom). Although a group trend exists in the effect of electronic temperature on the atomic forces, the change in free energy is always negative as it is calculated from higher-order terms of the free-energy-perturbation formula.

We have also analyzed vacancy contributions to the free energy, which can be mostly neglected in terms of the bulk thermodynamic properties. However, the Gibbs energy of vacancy formation shows a strong temperature dependence. Here, we have used a previously-proposed non-Arrhenius-type temperature-dependence formulation. Such a formulation was shown to efficiently capture the key physical mechanism. Upon using it, we have found bcc refractories to have 2–3 times higher vacancy formation Gibbs energies compared to fcc elements, but with a similarly strong temperature dependence. Small changes in the vacancy formation Gibbs energy will affect vacancy kinetics, and thereby phase transformations, and hence an accurate prediction is crucial.

In conclusion, we have further refined our understanding of different contributions to the free energy. We have also improved the direct-upsampling methodology by additionally including contributions from vacancies, and comparing results on a homologous scale. In addition to the four previously

investigated elements [32], we have now also added four refractory elements, further expanding the *ab initio*-based thermodynamic database.

The necessary data are available in the DaRUS Repository and can be accessed via the repository [75]. The repository contains the training sets (VASP OUTCAR files), the low-MTPs and high-MTPs, the effective QH potentials, and the final thermodynamic database (properties) for the four unaries. In addition also the Gibbs energies of vacancy formation are included.

## ACKNOWLEDGMENTS

We would like to acknowledge Xi Zhang for valuable discussions on vacancy-formation free energies, and Li-Fang Zhu for providing the PBE-predicted melting temperatures of V and W. We also appreciate fruitful discussions with Nikolay Zotov. This project has received funding from the European Research Council (ERC) under the European Unions Horizon 2020 research and innovation program (Grant Agreement No. 865855). The authors acknowledge support by the state of Baden-Württemberg through bwHPC and the German Research Foundation (DFG) through Grant No. INST 40/575-1 FUGG (JUSTUS 2 cluster). The authors gratefully acknowledge the scientific support and HPC resources provided by the Erlangen National High Performance Computing Center (NHR@FAU) of the Friedrich-Alexander-Universität Erlangen-Nürnberg (FAU) under the NHR Project No. a102cb. NHR funding is provided by federal and Bavarian state authorities. NHR@FAU hardware is partially funded by the German Research Foundation (DFG) Grant No. 440719683. We also acknowledge EuroHPC JU for awarding us access to Vega at IZUM, Slovenia. B.G. acknowledges the support by the Stuttgart Center for Simulation Science (SimTech). P.S. would like to thank the Alexander von Humboldt Foundation for their support through the Alexander von Humboldt Postdoctoral Fellowship Program.

All authors designed the project, discussed the results, and wrote the manuscript. B.G. provided scripts; A.F., J.H.J., and P.S. performed the calculations.

The authors declare no competing interests.

- [1] F. Wang, G. H. Balbus, S. Xu, Y. Su, J. Shin, P. F. Rottmann, K. E. Knipling, J.-C. Stinville, L. H. Mills, O. N. Senkov *et al.*, Multiplicity of dislocation pathways in a refractory multiprincipal element alloy, *Science* **370**, 95 (2020).
- [2] O. N. Senkov, D. B. Miracle, K. J. Chaput, and J.-P. Couzinie, Development and exploration of refractory high entropy alloys—A review, *J. Mater. Res.* **33**, 3092 (2018).
- [3] P. Schade, H. Ortner, and I. Smid, Refractory metals revolutionizing the lighting technology: A historical review, *Int. J. Refract. Met. Hard Mater.* **50**, 23 (2015).
- [4] J. R. Davis, *ASM Specialty Handbook: Heat-Resistant Materials* (ASM International, Materials Park, OH, 1987), pp. 361–82.
- [5] S. Antusch, J. Reiser, J. Hoffmann, and A. Onea, Refractory materials for energy applications, *Energy Technol. (Weinheim, Ger.)* **5**, 1064 (2017).
- [6] O. El-Atwani, N. Li, M. Li, A. Devaraj, J. Baldwin, M. M. Schneider, D. Sobieraj, J. S. Wróbel, D. Nguyen-Manh, and S. A. Maloy, Outstanding radiation resistance of tungsten-based high-entropy alloys, *Sci. Adv.* **5**, eaav2002 (2019).
- [7] O. Senkov, G. Wilks, D. Miracle, C. Chuang, and P. Liaw, Refractory high-entropy alloys, *Intermetallics* **18**, 1758 (2010).
- [8] A. Glensk, B. Grabowski, T. Hickel, and J. Neugebauer, Understanding Anharmonicity in fcc Materials: From its Origin to *Ab Initio* Strategies beyond the Quasiharmonic Approximation, *Phys. Rev. Lett.* **114**, 195901 (2015).
- [9] P. Srinivasan, A. Shapeev, J. Neugebauer, F. Körmann, and B. Grabowski, Anharmonicity in bcc refractory elements: A detailed *ab initio* analysis, *Phys. Rev. B* **107**, 014301 (2023).
- [10] O. Hellman, P. Steneteg, I. A. Abrikosov, and S. I. Simak, Temperature dependent effective potential method for accurate

- free energy calculations of solids, *Phys. Rev. B* **87**, 104111 (2013).
- [11] D.-B. Zhang, T. Sun, and R. M. Wentzcovitch, Phonon Quasiparticles and Anharmonic Free Energy in Complex Systems, *Phys. Rev. Lett.* **112**, 058501 (2014).
- [12] Y. Lu, T. Sun, P. Zhang, P. Zhang, D.-B. Zhang, and R. M. Wentzcovitch, Premelting hcp to bcc Transition in Beryllium, *Phys. Rev. Lett.* **118**, 145702 (2017).
- [13] B. Grabowski, Y. Ikeda, P. Srinivasan, F. Körmann, C. Freysoldt, A. I. Duff, A. Shapeev, and J. Neugebauer, *Ab initio* vibrational free energies including anharmonicity for multicomponent alloys, *npj Comput. Mater.* **5**, 80 (2019).
- [14] See Supplemental Material at <http://link.aps.org/supplemental/10.1103/PhysRevB.107.174309> for additional material including detailed computational parameters, convergence tests and an additional figure corresponding to Fig. 10 for Ta.
- [15] A. Debernardi, M. Alouani, and H. Dreyssé, *Ab initio* thermodynamics of metals: Al and W, *Phys. Rev. B* **63**, 064305 (2001).
- [16] D. Orlikowski, P. Söderlind, and J. A. Moriarty, First-principles thermoelasticity of transition metals at high pressure: Tantalum prototype in the quasiharmonic limit, *Phys. Rev. B* **74**, 054109 (2006).
- [17] V. V. Hung, J. Lee, K. Masuda-Jindo, and L. Kim, First principles study of tantalum thermodynamics by the statistical moment method, *Comput. Mater. Sci.* **37**, 565 (2006).
- [18] X. Sha and R. E. Cohen, Lattice Dynamics and Thermodynamics of bcc vanadium at high pressures, *MRS Proc.* **987**, 9870508 (2006).
- [19] P. Souvatzis and O. Eriksson, *Ab initio* calculations of the phonon spectra and the thermal expansion coefficients of the 4d metals, *Phys. Rev. B* **77**, 024110 (2008).
- [20] Z.-L. Liu, L.-C. Cai, X.-R. Chen, Q. Wu, and F.-Q. Jing, *Ab initio* refinement of the thermal equation of state for bcc tantalum: The effect of bonding on anharmonicity, *J. Phys.: Condens. Matter* **21**, 095408 (2009).
- [21] S. Ono, First-principles molecular dynamics calculations of the equation of state for tantalum, *IJMS* **10**, 4342 (2009).
- [22] Z.-Y. Zeng, C.-E. Hu, L.-C. Cai, X.-R. Chen, and F.-Q. Jing, Lattice dynamics and thermodynamics of molybdenum from first-principles calculations, *J. Phys. Chem. B* **114**, 298 (2010).
- [23] Z.-C. Guo, F. Luo, X.-L. Zhang, C.-Y. Yuan, C.-A. Liu, and L.-C. Cai, First-principles calculations of elastic, phonon and thermodynamic properties of W, *Mol. Phys.* **114**, 3430 (2016).
- [24] T. Degg, V. Razumovskiy, L. Romaner, G. Kresse, P. Puschnig, and J. Spitaler, Thermal expansion coefficient of WRe alloys from first principles, *Phys. Rev. B* **96**, 035148 (2017).
- [25] R. Bodlos, T. Degg, A. V. Ruban, M. Dehghani, L. Romaner, and J. Spitaler, *Ab initio* investigation of the atomic volume, thermal expansion, and formation energy of WTi solid solutions, *Phys. Rev. Mater.* **5**, 043601 (2021).
- [26] A. Forslund and A. Ruban, *Ab initio* surface free energies of tungsten with full account of thermal excitations, *Phys. Rev. B* **105**, 045403 (2022).
- [27] B. Grabowski, L. Ismer, T. Hickel, and J. Neugebauer, *Ab initio* up to the melting point: Anharmonicity and vacancies in aluminum, *Phys. Rev. B* **79**, 134106 (2009).
- [28] A. I. Duff, T. Davey, D. Korbacher, A. Glensk, B. Grabowski, J. Neugebauer, and M. W. Finnis, Improved method of calculating *ab initio* high-temperature thermodynamic properties with application to ZrC, *Phys. Rev. B* **91**, 214311 (2015).
- [29] Y. Sun, M. I. Mendeleev, F. Zhang, X. Liu, B. Da, C.-Z. Wang, R. M. Wentzcovitch, and K.-M. Ho, *Ab initio* melting temperatures of bcc and hcp iron under the earth's inner core condition, *Geophys. Res. Lett.* **50**, e2022GL102447 (2023).
- [30] N. Lopanitsyna, C. Ben Mahmoud, and M. Ceriotti, Finite-temperature materials modeling from the quantum nuclei to the hot electron regime, *Phys. Rev. Mater.* **5**, 043802 (2021).
- [31] Y. Zhou, P. Srinivasan, F. Körmann, B. Grabowski, R. Smith, P. Goddard, and A. I. Duff, Thermodynamics up to the melting point in a TaVCrW high entropy alloy: Systematic *ab initio* study aided by machine learning potentials, *Phys. Rev. B* **105**, 214302 (2022).
- [32] J. H. Jung, P. Srinivasan, A. Forslund, and B. Grabowski, High-accuracy thermodynamic properties to the melting point from *ab initio* calculations aided by machine-learning potentials, *npj Comput. Mater.* **9**, 3 (2023).
- [33] A. V. Shapeev, Moment tensor potentials: A class of systematically improvable interatomic potentials, *Multiscale Model. Simul.* **14**, 1153 (2016).
- [34] R. W. Zwanzig, High-temperature equation of state by a perturbation method. I. Nonpolar gases, *J. Chem. Phys.* **22**, 1420 (1954).
- [35] J. P. Perdew, K. Burke, and M. Ernzerhof, Generalized Gradient Approximation Made Simple, *Phys. Rev. Lett.* **77**, 3865 (1996).
- [36] B. Grabowski, T. Hickel, and J. Neugebauer, Formation energies of point defects at finite temperatures, *Phys. Status Solidi B* **248**, 1295 (2011).
- [37] X. Zhang, B. Grabowski, F. Körmann, C. Freysoldt, and J. Neugebauer, Accurate electronic free energies of the 3d, 4d, and 5d transition metals at high temperatures, *Phys. Rev. B* **95**, 165126 (2017).
- [38] N. D. Mermin, Thermal Properties of the Inhomogeneous Electron Gas, *Phys. Rev.* **137**, A1441 (1965).
- [39] A. Glensk, B. Grabowski, T. Hickel, and J. Neugebauer, Breakdown of the Arrhenius Law in Describing Vacancy Formation Energies: The Importance of Local Anharmonicity Revealed by *Ab Initio* Thermodynamics, *Phys. Rev. X* **4**, 011018 (2014).
- [40] Y. Gong, B. Grabowski, A. Glensk, F. Körmann, J. Neugebauer, and R. C. Reed, Temperature dependence of the Gibbs energy of vacancy formation of fcc Ni, *Phys. Rev. B* **97**, 214106 (2018).
- [41] P.-W. Ma and S. L. Dudarev, Universality of point defect structure in body-centered cubic metals, *Phys. Rev. Mater.* **3**, 013605 (2019).
- [42] P. M. Derlet, D. Nguyen-Manh, and S. L. Dudarev, Multiscale modeling of crowdion and vacancy defects in body-centered-cubic transition metals, *Phys. Rev. B* **76**, 054107 (2007).
- [43] H. Sun and L. K. Béland, Statistical distribution of spontaneous recombination radii of Frenkel pairs in FCC and BCC metals, *Acta Mater.* **229**, 117814 (2022).
- [44] P. E. Blöchl, Projector augmented-wave method, *Phys. Rev. B* **50**, 17953 (1994).
- [45] G. Kresse and J. Hafner, *Ab initio* molecular dynamics for liquid metals, *Phys. Rev. B* **47**, 558 (1993); *Ab initio* molecular-dynamics simulation of the liquid-metal–amorphous-semiconductor transition in germanium, **49**, 14251 (1994); G. Kresse and J. Furthmüller, Efficiency of *ab-initio*

- total energy calculations for metals and semiconductors using a plane-wave basis set, *Comput. Mater. Sci.* **6**, 15 (1996); Efficient iterative schemes for *ab initio* total-energy calculations using a plane-wave basis set, *Phys. Rev. B* **54**, 11169 (1996).
- [46] G. Kresse and D. Joubert, From ultrasoft pseudopotentials to the projector augmented-wave method, *Phys. Rev. B* **59**, 1758 (1999).
- [47] M. Methfessel and A. T. Paxton, High-precision sampling for Brillouin-zone integration in metals, *Phys. Rev. B* **40**, 3616 (1989).
- [48] H. J. Monkhorst and J. D. Pack, Special points for Brillouin-zone integrations, *Phys. Rev. B* **13**, 5188 (1976).
- [49] I. S. Novikov, K. Gubaev, E. V. Podryabinkin, and A. V. Shapeev, The MLIP package: Moment tensor potentials with MPI and active learning, *Mach. Learn.: Sci. Technol.* **2**, 025002 (2021).
- [50] A. Dinsdale, SGTE data for pure elements, *Calphad* **15**, 317 (1991).
- [51] P. Haas, F. Tran, and P. Blaha, Calculation of the lattice constant of solids with semilocal functionals, *Phys. Rev. B* **79**, 085104 (2009).
- [52] P. Haas, F. Tran, P. Blaha, K. Schwarz, and R. Laskowski, Insight into the performance of GGA functionals for solid-state calculations, *Phys. Rev. B* **80**, 195109 (2009).
- [53] L. F. Zhu, P. Srinivasan, Y. Gong, T. Hickel, F. Körmann, B. Grabowski, and J. Neugebauer (unpublished).
- [54] W. M. Haynes, D. R. Lide, and T. J. Bruno (eds.), *CRC Handbook of Chemistry and Physics*, eighty-eighth ed. (CRC Press, Boca Raton, FL, 2007).
- [55] N. D. Milošević, G. S. Vuković, D. Z. Pavičić, and K. D. Maglić, Thermal properties of tantalum between 300 and 2300 K, *Int. J. Thermophys.* **20**, 1129 (1999).
- [56] K. Wang and R. R. Reeber, The role of defects on thermophysical properties: Thermal expansion of V, Nb, Ta, Mo and W, *Mater. Sci. Eng., R* **23**, 101 (1998).
- [57] Y. S. Touloukian, R. Kirby, R. Taylor, and P. Desai, *Thermal Expansion Metallic Elements and Alloys*, edited by Y. S. Touloukian and C. Y. Ho, Thermophysical Properties of Matter - the TPRC Data Series Vol. 12 (IFI/Plenum, New York, 1975), pp. 1–1348.
- [58] F. H. Featherston and J. R. Neighbours, Elastic Constants of Tantalum, Tungsten, and Molybdenum, *Phys. Rev.* **130**, 1324 (1963).
- [59] E. Walker, Anomalous temperature behaviour of the shear elastic constant  $C_{44}$  in vanadium, *Solid State Commun.* **28**, 587 (1978).
- [60] N. Soga, Comparison of measured and predicted bulk moduli of tantalum and tungsten at high temperatures, *J. Appl. Phys.* **37**, 3416 (1966).
- [61] E. Walker and P. Bujard, Anomalous temperature behaviour of the shear elastic constant  $C_{44}$  in tantalum, *Solid State Commun.* **34**, 691 (1980).
- [62] J. M. Dickinson and P. E. Armstrong, Temperature dependence of the elastic constants of molybdenum, *J. Appl. Phys.* **38**, 602 (1967).
- [63] P. Bujard, R. Sanjines, E. Walker, J. Ashkenazi, and M. Peter, Elastic constants in Nb-Mo alloys from zero temperature to the melting point: Experiment and theory, *J. Phys. F: Met. Phys.* **11**, 775 (1981).
- [64] R. Lowrie and A. M. Gonas, Single-crystal elastic properties of tungsten from 24° to 1800 °C, *J. Appl. Phys.* **38**, 4505 (1967).
- [65] B. Grabowski, T. Hickel, and J. Neugebauer, *Ab initio* study of the thermodynamic properties of nonmagnetic elementary fcc metals: Exchange-correlation-related error bars and chemical trends, *Phys. Rev. B* **76**, 024309 (2007).
- [66] L.-F. Zhu, B. Grabowski, and J. Neugebauer, Efficient approach to compute melting properties fully from *ab initio* with application to Cu, *Phys. Rev. B* **96**, 224202 (2017).
- [67] J. Byggmästar, K. Nordlund, and F. Djurabekova, Gaussian approximation potentials for body-centered-cubic transition metals, *Phys. Rev. Mater.* **4**, 093802 (2020).
- [68] T. Korhonen, M. J. Puska, and R. M. Nieminen, Vacancy-formation energies for fcc and bcc transition metals, *Phys. Rev. B* **51**, 9526 (1995).
- [69] P. A. Korzhavyi, I. A. Abrikosov, B. Johansson, A. V. Ruban, and H. L. Skriver, First-principles calculations of the vacancy formation energy in transition and noble metals, *Phys. Rev. B* **59**, 11693 (1999).
- [70] P. Söderlind, L. H. Yang, J. A. Moriarty, and J. M. Wills, First-principles formation energies of monovacancies in bcc transition metals, *Phys. Rev. B* **61**, 2579 (2000).
- [71] T. R. Mattsson, N. Sandberg, R. Armiento, and A. E. Mattsson, Quantifying the anomalous self-diffusion in molybdenum with first-principles simulations, *Phys. Rev. B* **80**, 224104 (2009).
- [72] H. Ullmaier (ed.), *Atomic Defects in Metals*, Landolt-Börnstein - Group III Condensed Matter Vol. 25 (Springer-Verlag, Berlin/Heidelberg, 1991), pp. 141, 174, 162, 181.
- [73] B. Grabowski, Towards *Ab Initio* assisted materials design: DFT based thermodynamics up to the melting point, Ph.D. thesis, University of Paderborn, 2009.
- [74] J. Zhuang, H. Wang, Q. Zhang, and R. M. Wentzcovitch, Thermodynamic properties of  $\epsilon$ -Fe with thermal electronic excitation effects on vibrational spectra, *Phys. Rev. B* **103**, 144102 (2021).
- [75] A. Forslund, J. H. Jung, P. Srinivasan, and B. Grabowski, “Data for: Thermodynamic properties on the homologous temperature scale from direct upsampling: Understanding electron-vibration coupling and thermal vacancies in bcc refractory metals (2023)”, doi: 10.18419/darus-3339.